Uncertainty and global sensitivity analysis of bladed disk statics with material anisotropy and root geometry variations

Article (Accepted Version)

Uncertainty And Global Sensitivity Analysis Of Bladed Disks Statics With Material Anisotropy And Root Geometry Variations

Rahul Rajasekharan[a] and E. Petrov[a,*]

[a]*School of Engineering and Informatics, University of Sussex, Brighton, UK, BN19RH*

Abstract

Monocrystalline blades used in gas turbines exhibit material anisotropy and the orientation of the anisotropy axis affects the deformation of the bladed disk. Considering the orientation of the anisotropy axis as a random design parameter, the uncertainty and sensitivity analysis for static blade deformations are presented for the first time. The following two cases are analysed using a realistic bladed disk model with friction contacts: (i) deformation of the tuned bladed disks considering the uncertainty in anisotropy orientation and variations in fir tree root geometry and (ii) deformation of mistuned bladed disks with uncertain blade crystal orientations. For efficient uncertainty and sensitivity analysis, the applicability of the following surrogate models are explored: (i) an ensemble of regression trees (Random Forest) and (ii) gradient-based polynomial chaos expansion. Faster convergence in statistical characteristics has been obtained using a surrogate model compared to that obtained from finite element model based Monte Carlo simulation. From sensitivity analysis, it has been inferred that the uncertainty in static displacements of a blade in a bladed disk is primarily due to the uncertainty in anisotropy angles of that blade itself and secondarily due to the interaction of different blade anisotropy angles.

Keywords: Anisotropy, Bladed disk, Single crystal blades, Surrogate modelling, Polynomial chaos, uncertainty analysis, sensitivity analysis.

*Corresponding author: email address: Y.Petrov@sussex.ac.uk

September 13, 2019

Abbreviations

GSA	Global Sensitivity Analysis
CS	Coordinate System
FE	Finite Element
PCE	Polynomial Chaos Expansion
MCS	Monte Carlo Simulation
gradPCE	gradient based Polynomial Chaos Expansion
STD	Standard deviation
UA	Uncertainty analysis
RF	Random Forest
MSE	Mean Square Error
MAE	Mean Absolute Error

Nomenclature

α, β, ζ	Crystal anisotropy angles
$\boldsymbol{\sigma}$	Cauchy stress tensor
$\boldsymbol{\epsilon}$	Strain tensor
$\mathbf{S}$	Material Compliance matrix
$\mathbf{E}$	Material Elasticity matrix
$\mathbf{T}$	Coordinate transformation matrix
$\boldsymbol{K}$	Global stiffness matrix
$\boldsymbol{k}^e$	Element stiffness matrix
$\boldsymbol{r}$	Rotation vector defining crystal axis
$\boldsymbol{F}_{nln}$	Non-linear force vector
$\boldsymbol{P}$	Static force vector
ξ	Random variable
y	Stochastic function
n	Dimension of random space
p	Order of polynomial chaos expansion
ψ	Polynomial basis function
ρ	Probability density function

1. Introduction

1.1. Background and Motivation.

The response of bladed disks to various mechanical and thermal loads depends on a multitude of geometric, material and loading parameters. The values of some of these parameters are uncertain especially when taking into account the varying operating conditions of a gas turbine engine. To ensure the safe operation of the gas turbine engine, it is essential to account for the uncertainty in input design parameters to assess the deformation of the structure accurately.

The nickel–based–alloy blades in high-pressure turbine stage of modern gas turbine engines are monocrystalline, the crystallographic orientations of which influence the mechanical properties of the blades [1]. Scatter in crystal orientation arises from inaccuracies in the casting process of single crystal blades which results in scatter in material properties of blades in a bladed disk. There are few articles in the literature that investigate the effect of blade anisotropy orientation on blade deformation. Kaneko [2], Manetti et al. [3] and Wen et al. [4] studied the effects of variation in crystal orientation on natural frequencies of blades. Savage [5] investigated the effects of crystal orientation on elastic

stresses in single crystal blades. While Arakere et al. [6] studied the effects of crystal orientation on fatigue life of bladed disk, Weiss et al. [7] investigated the effects of crystal orientation on low cycle fatigue and creep damage based lifetime of monocrystal blades using probabilistic finite element analysis based on Monte-Carlo-Simulation (MCS) techniques.

In a bladed disk assembly, the blade-disk joints are the most critically loaded part, and therefore, a detailed analysis of the stresses in the region close to the joint is mandated for the lifetime certification of aero-engine turbine disk [8]. The most common design for blade root joints is dovetail and fir tree joints. While dovetail joints are commonly used to secure compressor blades to disks, fir tree root joints are widely used to fit turbine blades to disks. As far as the design of the joints is concerned, it is necessary to ensure that the service life of the bladed disk is not limited by the failure of the joint. Several studies that consider the deformation and stresses on bladed disk joints are available in the literature for both dovetail and fir tree joints [9–15]. There are few studies investigating the effects of fir tree geometry on stresses developed in the turbine disk. Meguid et al. [8] studied the effect of variation in certain key geometric features of the fir tree, such as the number of teeth, flank angle and flank length, on von-Mises stresses on disk slot. There are articles in the literature that deal with the optimization of the fir tree root joint geometry with the objective of reducing the stresses in the joint [16–21].

Random errors in manufacturing process introduce variability in the geometry of the blade root and the disk slots. Due to the variability in blade and disk geometry within the tolerance limits, the contact area at joints could be higher or lower than that of the nominal design geometry. The variation in contact areas affects the magnitude of contact pressure, and therefore, the contact stresses at the bladed disk root joint. In his investigation, Zboinski [22] found that manufacturing deviations can significantly change the contact stresses and concluded that neglecting the deviations in geometry can result in an erroneous estimation of the contact stresses on fir tree joints. Deshpande et al. [23] addressed the issue of variation in geometry of fir tree tooth by parametrizing the geometry using parametric CAD models. Qin et al. [24] studied the effect of geometry mismatch in fir tree joints on the natural frequency of blade by varying the surfaces where contact or gap exists. Avalos et al. [25] investigated the effects of blade-disk interface mistuning on the force response amplification of bladed disks.

To maximize the efficiency of gas-turbine engines, clearance between the blades and turbine casing must be minimized to reduce tip leakage. Modern gas-turbine engines use an abradable material seal which allows the formation of an optimal gap between blades and casing during the initial runs. Even though this technique has proved to be effective in minimizing the radial gap, there are two main concerns associated with it: (i) the possibility of the abradable material sticking to the blades, thereby, inducing turbulence in the gas flow, and (ii) the phenomenon of blade wear due to friction between blades and abradable material [26]. However for a mistuned bladed disk with significant scatter in blade mechanical properties, each blade will have marginally different radial elongation which then precludes the possibility of creating an optimal gap. In this case, the blade with largest radial elongation will determine the amount of

abradable material removed, thereby, creating a suboptimal tip-casing gap for other blades in the bladed disk. To minimize the amount of abradable material removed and to maintain the optimal tip-casing gap for all blades, there is a need to quantify the scatter in static deformation of mistuned bladed disks due to scattering in material properties of the blades.

Uncertainty analysis (UA) often requires numerous evaluations of computational models based on the sampling of input parameter space. Uncertainty analysis using conventional Monte Carlo methods are prohibitive when using high-fidelity FE models. Therefore, in order to perform UA, the use of reduced order FE models [27] or surrogate models that can closely approximate the FE model is very attractive. Following are some of the approaches used to construct surrogate models: (i) polynomial regression (ii) polynomial chaos (iii) kriging and (iv) supervised learning methods such as random forest, support vector machines (SVM) and artificial neural networks.

The structure of the input parameter space is one of the deciding factors in the choice of surrogate models. When the input parameter space is n dimensional real space, the choice of polynomial chaos or kriging is recommended. For situations when the input parameter set includes both categorical and continuous variables, random forest (RF) is a viable option [28]. RF is a predictive model constituted by an ensemble of binary regression trees. A regression tree divides the input parameter space into distinct and non-overlapping regions where the dependent variable is approximated by a constant value. The input-output data obtained from FE model evaluations are randomly partitioned into a training set and test set. To train the RF model, each regression tree in the ensemble is trained on a random subset of the training data where the subset is obtained by bootstrap sampling. The predictions from individual regression trees are then aggregated by averaging. This so-called bagging (or bootstrap aggregating) procedure significantly reduces the variance in prediction associated with individual regression trees. The performance of the RF model is validated using data in the test set. RF methods have been applied with varying degree of success to regression and classification problems arising in different fields ranging from fluid flow modeling [29] to medical prognosis [17]. Ling and Templeton [30] investigated the use of three different data-driven algorithms including RF and support vector machines [31] to identify regions in a fluid flow where the inaccuracy of Reynolds Averaged Navier Stokes (RANS) models is high. They concluded that data-driven algorithms provide a substantial improvement over conventional RANS error detection methods and showed the performance of RF to be superior compared to the other algorithms used. Trehan et al. [32] used RF-based regression to model the error introduced by reduced order models of parametrized dynamical systems. For uncertainty quantification, the possibility of using data-driven algorithms such as RF to avoid Monte Carlo Simulations (MCS) using high-fidelity FE models has not been adequately investigated in the existing literature.

The surrogate models based on polynomial chaos expansion (PCE) have been studied extensively for quantifying uncertainty in dynamic systems [33, 34]. The main feature of PCE is the decomposition of output response into a linear combination of deterministic and stochastic components. The computational effort in obtaining PCE is associated with the calculation of coefficients in the expan-

sion based on a finite number of evaluations of the deterministic FE model of the bladed disks. Panunzio et al. [35] used PCE to study the effects of uncertainty in the tip-casing gap on non-linear normal modes of turbine blades. Considering the modal stiffness of blades as random variables, Sinha [36] obtained the statistics of forced response for mistuned bladed disks using PCE. Rahul and Petrov [37] used gradient enhanced polynomial chaos expansion to obtain the statistical characteristics of scattering in static displacements due to random anisotropy orientation of blades in bladed disks with material anisotropy mistuning.

The aim of sensitivity analysis is to obtain a measure of output variation with respect to system input parameter variations [38]. It provides valuable insights on how scattering in individual design parameters influences the response of the structure. The two approaches to sensitivity analysis are (i) local sensitivity analysis (LSA), and (ii) global sensitivity analysis (GSA). The aim of LSA is to calculate sensitivity coefficients, i.e. first or higher order derivatives of response with respect to design parameters, at a chosen point in the domain of variation of the design variables. There are only a few articles in the literature that deal with sensitivity analysis of bladed disks. Petrov [39] derived analytical expressions for first and second-order sensitivity derivatives, with respect to parameters of friction contact interface, frequency and level of excitation forces for the non-linear forced response of a structure. In reference [40], he used sensitivity derivatives to calculate uncertainty ranges and stochastic characteristics of forced response for the non-linear vibrations of bladed disks with friction and gap contact interfaces.

LSA cannot capture the higher order interactions between different input parameters if it exist in the model. Therefore, for sensitivity analysis of non-linear, non-additive models GSA is recommended [41].

The objective of GSA is to quantify the variation in system output with respect to variations in input parameters over the entire domain of variation. Methods available to perform GSA can be classified into the following two groups [42, 43]: (i) regression based methods such as Pearson or Spearman correlation coefficient which are suitable for linear (Pearson) or monotonic (Spearman) models and, (ii) variance based techniques such as Fourier Amplitude Sensitivity Analysis (FAST) [44] and Sobol indices [45]. The idea behind variance decomposition methods is to partition the output variance into contributions from each of the input parameters.

Variance decomposition based GSA is useful to identify the subset of the input parameters that contribute significantly to output variance [38]. This information can be used to reduce the dimensionality of the input parameter space, and therefore, the computational cost for uncertainty analysis. Kala and Vales [41] used Sobol indices to study the influence of initial geometric imperfections and residual stresses on lateral-torsional buckling resistance of I-beams. To reduce the computational cost involved in calculating Sobol indices using conventional Monte Carlo Simulation (MCS), they used a polynomial approximation of the output. Hesse et al. [42] used Sobol indices to identify important design parameters that influence the maximum deformation of an automotive structure in order to reduce the complexity involved in designing the structure for crashworthiness. They used a response surface approximation based on SVM to reduce the computational cost involved in calculating Sobol indices using MCS. Sudret

[46] derived expressions for calculation of Sobol indices analytically from the expansion coefficients of PCE. While performing uncertainty analysis of a coupled flow-thermo-mechanical model of a low-pressure turbine rotor of gas turbine engines, Antinori et al. [47] used Sobol indices to reduce the dimensionality of the input parameter space by identifying most influential design parameters in the secondary air system of the aero-engine.

1.2. Objective and scope of the paper.
In this paper, the effects on the static deformation of bladed disks due to uncertainty in anisotropy orientation of monocrystalline blades, together with the effects of root joints geometry variations, are investigated for the first time using a realistic bladed disk sector model. Using a random forest-based surrogate model, the uncertainty in static deformation of tuned bladed disks caused by scattering in anisotropy orientation and root geometry variation is quantified. The choice of the surrogate model depends on, among other factors, the type of design parameters. On one hand, when the design parameters are a combination of categorical and continuous variables, a RF-based model is an attractive option especially because of the minimum number of model parameters compared to that of other data-driven models like neural networks or support vector machines. On the other hand, when the design parameter space is composed of only continuous variables, anisotropy angles in the case of mistuned bladed disk, the choice is mainly between polynomial chaos expansion and kriging. In this paper, for uncertainty and sensitivity analysis of the mistuned bladed disk, gradient enhanced polynomial chaos expansion is used considering its ease of implementation and the straight forward calculation of statistical characteristics and global sensitivity measures for output function. Global sensitivity analysis for blade displacements is presented for the case of the mistuned bladed disk with several blades having random anisotropy axis orientation. Using global sensitivity analysis, the rank order of importance of anisotropy angles considering static displacements of the mistuned bladed disk is obtained for the first time.

The rest of the article is structured in the following manner. The mathematical formulation associated with the modelling of static deformation of bladed disk with material anisotropy is presented in Section 2.1 which is followed by a section on mathematical formulation for obtaining local sensitivity of blade displacements w.r.t crystal orientation of blades. In section 3, the theoretical aspects the two surrogate models, i.e. Random Forest and Polynomial chaos expansion, is discussed. The mathematical formulation for a variance-based global sensitivity analysis is presented in Section 4. The finite elements model of bladed disks used in this study are introduced in Section 5.1. The numerical results for the tuned bladed disk with different root geometry variants are presented in Section 5.2 which is followed by Section 5.3 where the results for the mistuned bladed disk are presented. Finally, in Section 6, the conclusions obtained from the present study are given.

The examples of application of the methodology developed here are provided for realistic bladed disk models shown in Fig. 1(a). The statistic characteristics are estimated using the realistic statistical data for variation of three material angles: the primary angle and two secondary angles of the anisotropy orientation. The blade anisotropic material properties and the friction coefficient values at

the contact interfaces of blade-disk joints correspond to the temperatures at the operating regime of the analyzed bladed disk.

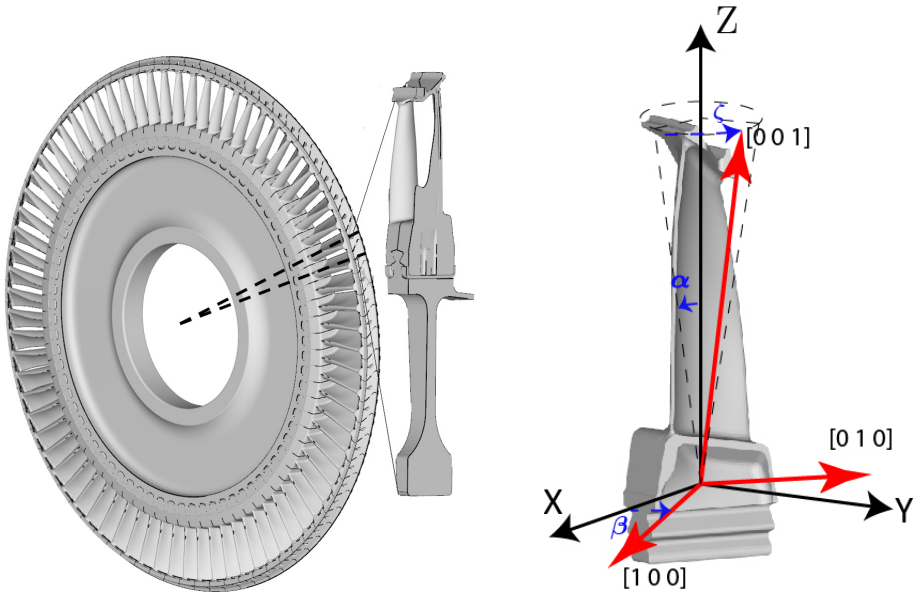

(a) (b)

Figure 1: Figure showing (a) bladed disk and (b) blade anisotropy angles.

2. FINITE ELEMENT ANALYSIS OF BLADED DISK AND CALCULATION OF LOCAL SENSITIVITIES

2.1. Modelling of bladed disks with anisotropic blades

Fig. 1(a) shows an example of a realistic bladed disk model. The single crystal nickel alloy blades have face-centred-cubic structure, the material properties of which are different along the three orthogonal directions of the crystal axis. The rotation of crystal axis is represented by coordinate system (CS) rotation, defined by three angles, α, β and ζ as shown in Fig.1(b). These angles are obtained from the manufacturer of the blades and are defined as below:

- α - The angle between crystallographic direction [001] and Z–axis (radial direction). Its is also called the primary angle and is always positive.
- β - The angle between crystallographic direction [100] and X–axis (axial direction) or angle between crystallographic direction [010] and X–axis depending on whichever is smaller. It is also called the secondary angle and is always positive.
- ζ - The angle of rotation defining the orientation of crystallographic direction [001] with respect to the Z–axis.

These angles are similar to Euler angles in that it has a defined sequence of rotation which is α, followed by β and ζ, but the admissible range for each angle is restricted by the manufacturer. The range of value of the angles and its prob-

ability distribution is not presented in the article to maintain the confidentiality of the information obtained from the industry.

The elastic stress–strain relationship for orthotropic materials is given by Eq.(1)

$$\{\boldsymbol{\epsilon}\} = [\mathbf{S}]\{\boldsymbol{\sigma}\} \quad \text{or} \quad \{\boldsymbol{\sigma}\} = [\mathbf{E}]\{\boldsymbol{\epsilon}\} \tag{1}$$

where, $\boldsymbol{\sigma}$ and $\boldsymbol{\epsilon}$ are stress tensor and strain tensor in the crystal CS, $[\mathbf{E}] = [\mathbf{S}]^{-1}$ is the elasticity matrix written in the crystal CS. The compliance matrix, $[\mathbf{S}]$ expressed in the CS coinciding with the anisotropy axes is written as:

$$[\mathbf{S}] = \begin{bmatrix} \frac{1}{E_x} & \frac{-\nu_{xy}}{E_x} & \frac{-\nu_{xz}}{E_x} & 0 & 0 & 0 \\ \frac{-\nu_{yx}}{E_y} & \frac{1}{E_y} & \frac{-\nu_{yz}}{E_y} & 0 & 0 & 0 \\ \frac{-\nu_{zx}}{E_z} & \frac{-\nu_{zy}}{E_z} & \frac{1}{E_z} & 0 & 0 & 0 \\ 0 & 0 & 0 & \frac{1}{G_{yz}} & 0 & 0 \\ 0 & 0 & 0 & 0 & \frac{1}{G_{xz}} & 0 \\ 0 & 0 & 0 & 0 & 0 & \frac{1}{G_{xy}} \end{bmatrix} \tag{2}$$

where, ν is Poisson's ratio, E is Young's modulus and G is shear modulus.

In order to perform FE analysis of a bladed disk, the stress-strain relationship (Eq. 1) has to be transformed to a global CS. The coordinate transformation for stresses in crystal coordinate system to stresses in global CS is given by Eq. (3)

$$\{\boldsymbol{\sigma}'\} = [\mathbf{T}_\sigma]\{\boldsymbol{\sigma}\} \tag{3}$$

Similarly, strains could be transformed:

$$\{\boldsymbol{\epsilon}'\} = [\mathbf{T}_\epsilon]\{\boldsymbol{\epsilon}\} \tag{4}$$

where, $\boldsymbol{\sigma}'$ and $\boldsymbol{\epsilon}'$ are stresses and strains in global CS, $[\mathbf{T}_\sigma]$ and $[\mathbf{T}_\epsilon]$ are transformation matrices for stress and strain respectively. These matrices are formed from direction cosines of blade anisotropy CS while allowing for orientation of blade stacking axis in the bladed disk. From Eqs.(1), (3) and (4), the elasticity matrix in global CS could be written as in Eq.(5)

$$[\mathbf{E}'] = [\mathbf{T}_\epsilon][\mathbf{E}][\mathbf{T}_\sigma]^{-1} \tag{5}$$

and a finite element matrices comprising the blades are calculated as:

$$\boldsymbol{k}^e = \int_{V^e} \boldsymbol{B}^T \mathbf{E}'(\boldsymbol{r}_j)\boldsymbol{B}\, \mathrm{d}V^e,\ e = 1, \ldots, N_{el} \tag{6}$$

where, $\boldsymbol{r}_j = \{r_x, r_y, r_z\}$ is the rotation vector defining the orientation of crystallographic axis of the j^{th} blade in the bladed disk, $\boldsymbol{B}$ is the strain-displacement matrix which include the derivative of quadratic shape functions, V^e is the element volume and N_{el} is the total number of elements.

For non-linear static analysis, the solution is obtained by solving the governing equation of the bladed disk:

$$\boldsymbol{K}(\boldsymbol{r}_1, \ldots, \boldsymbol{r}_j, \ldots, \boldsymbol{r}_{N_B})\boldsymbol{x} + \boldsymbol{F}_{nln}(\boldsymbol{x}) = \boldsymbol{P} \tag{7}$$

where, N_B is the number of blades in the bladed disk, $\boldsymbol{F}_{nln}(\boldsymbol{x})$ is the vector of non-linear internal forces which takes into account non-linear friction contact interaction at blade-disk contact interfaces and geometric non-linearities due to effect of centrifugal force, $\boldsymbol{P}$, is the vector of static external forces and the global stiffness matrix, $\boldsymbol{K}$, of the bladed disk is obtained by assembling the element stiffness matrices $\boldsymbol{k}^e$. Eqn.(7) is solved using Newton-Raphson iteration method:

$$\boldsymbol{x}_{k+1} = \boldsymbol{x}_k + \boldsymbol{J}\left(\boldsymbol{K}\boldsymbol{x}_k + \boldsymbol{F}_{nln}(\boldsymbol{x}_k) - \boldsymbol{P}\right) \tag{8}$$

where $\boldsymbol{J} = \left(\boldsymbol{K} + \frac{\partial \boldsymbol{F}_{nln}}{\partial \boldsymbol{x}}\right)$ is the Jacobian of Eq.(7) and $\boldsymbol{x}_k$, $\boldsymbol{x}_{k+1}$ are the approximate solutions obtained at the k^{th} and $(k+1)^{\text{th}}$ iteration respectively. The iterative process terminates when the solution reaches sufficient accuracy, ϵ; for e.g. when $||\boldsymbol{x}_{k+1} - \boldsymbol{x}_k|| < \epsilon$.

2.2. Sensitivity to blade material anisotropy

The equation for displacement sensitivity corresponding to the j^{th} blade anisotropy is obtained by differentiating Eq.(7) with respect to anisotropy orientation vector, $\boldsymbol{r}_j$:

$$\frac{\partial \boldsymbol{K}}{\partial \boldsymbol{r}_j}\boldsymbol{x} + \boldsymbol{K}\frac{\partial \boldsymbol{x}}{\partial \boldsymbol{r}_j} + \frac{\partial \boldsymbol{F}_{nln}}{\partial \boldsymbol{x}}\frac{\partial \boldsymbol{x}}{\partial \boldsymbol{r}_j} = 0 \tag{9}$$

rearranging terms in Eq.(9):

$$\left(\boldsymbol{K} + \frac{\partial \boldsymbol{F}_{nln}}{\partial \boldsymbol{x}}\right)\frac{\partial \boldsymbol{x}}{\partial \boldsymbol{r}_j} = \boldsymbol{J}\frac{\partial \boldsymbol{x}}{\partial \boldsymbol{r}_j} = -\frac{\partial \boldsymbol{K}}{\partial \boldsymbol{r}_j}\boldsymbol{x}^*,\ j = 1, \ldots, N_B \tag{10}$$

where $\boldsymbol{x}^*$ is solution vector obtained by solving Eq.(7), $\partial \boldsymbol{x}/\partial \boldsymbol{r}_j$ are the required sensitivities and N_B is the total number of blades in the bladed disk.

The sensitivities of the element stiffness matrix with respect to crystal orientation is calculated from Eq.(11)

$$\frac{\partial \boldsymbol{k}^e}{\partial \boldsymbol{r}_j} = \int_{V^e} \boldsymbol{B}^T \frac{\partial \mathbb{E}'}{\partial \boldsymbol{r}_j}\boldsymbol{B}\, \mathrm{d}V^e \tag{11}$$

The sensitivities of the element stiffness matrix is assembled using conventional FE assembling procedure to obtain the sensitivities of global stiffness matrix, $\partial \boldsymbol{K}/\partial \boldsymbol{r}_j$, in the right hand side of Eq.(10).

The Jacobian matrix, $\boldsymbol{J}$ in Eq.(10) is evaluated while solving Eq.(7), and hence, the computational cost involved in calculation of sensitivities is kept to a minimum. The sensitivities are calculated for all blades of interest in the bladed disk.

3. Surrogate modelling in uncertainty analysis of bladed disks

The present paper investigates the use of efficient surrogate models as an alternative for computationally intensive Monte Carlo simulations for uncertainty analysis of high-fidelity FE models of bladed disks. The choice of the surrogate model is dependent on different considerations including the type of design parameters. When the design parameter space is a combination of categorical variables, representing contact or no contact, and continuous variables, the random forest is a good choice considering that the underlying function is non-linear. In comparison to other data-driven models, such as support vector machines and neural networks, the number of model parameters associated with the random forest model are fewer. When the design parameter space is composed of only continuous variables, as in the case of the mistuned bladed disk with numerous random blade anisotropy angles, polynomial chaos expansion allows efficient uncertainty and global sensitivity analysis. Following two surrogate models used to obtain the statistics for blade deformation due to scattering in material anisotropy orientation are discussed in detail in this section: (i) random forest and (ii) polynomial chaos expansion.

3.1. Regression trees and random forest.

The computational cost associated with the UA of bladed disks could be significantly reduced by using computationally inexpensive surrogate models that can closely approximate the FE model. In this section, the idea behind a RF based surrogate model is explained. A random forest is a collection of randomized regression trees. Each regression tree consists of a series of criteria, about the input parameters, that split the input parameter space into different subspaces (or regions) where the response function (such as displacements or stresses) is then approximated by a constant value. Therefore, the regression tree could be thought of as a piecewise constant regression model.

To split a node in the regression tree into two daughter nodes, a splitting rule is chosen such that the weighted average of the error in the resulting nodes is minimum. In other words, the splitting condition that minimises the error $e_s(r)$ resulting from split s of the region r is chosen, where

$$e_s(r) = \frac{n_1}{n_r} e(r_1) + \frac{n_2}{n_r} e(r_2) \tag{12}$$

where n_1 and n_2 are the number of model evaluations that included in region r_1 and r_2 resulting from the binary split and n_r is the number of model evaluations associated with region r.

Two popular splitting criteria used to build regression trees are: (i) mean square error (MSE) and (ii) mean absolute error (MAE). For the MSE criterion the error of a node in the decision tree is the average of the squared differences between the instances of the response variable in the node and the node constant. The node constant in this case is the mean of all values for the set of model evaluations associated with the node. If $\{\boldsymbol{x}_i, y_i\} : i \in M_r$ is the set of model evaluations associated with a node that represents a region r in the input parameter space, where $\boldsymbol{x}_i$ is a vector of input parameters and y_i is the corresponding response value, the mean square error of the node is [48]:

$$e(r) = \frac{1}{n_r} \sum_{i \in M_r} (y_i - \bar{y})^2 \tag{13}$$

where, n_r is the number of model evaluations associated with the node, y_i is the output from the i^{th} evaluation of the FE model, $\bar{y}$ is the mean of all values of the model evaluations associated with the input parameter region r.

The MAE splitting criterion requires that the mean absolute deviation at all nodes be reduced to minimum. The value of the node constant that minimizes the mean absolute error of the node, for the set of model evaluations $\{\langle \boldsymbol{x}_i, y_i \rangle\}$ within the node, is given by the median of the response functions in the set. The mean absolute error associated with the node is given by

$$e(r) = \frac{1}{n_r} \sum_{i \in M_r} |(y_i - \hat{y})| \tag{14}$$

where, $\hat{y}$ is the median of the response function in the set M_r.

The set of model evaluations, $\{\boldsymbol{x}, y\} \in M$, is divided into the following two subsets: (i) training set (M_{train}) and (ii) test set (M_{test}). The training set is used to build the surrogate model and the test set is used to test the performance of the model on the cases that are not used at the stage of model building.

The application of regression trees is limited because these models suffer from high variance [49] and over-fitting. The primary reason for the high variance is the hierarchical nature of the process where an error in the higher nodes of the tree affects all the nodes below it. By averaging the regression estimate of an ensemble of regression trees, the RF algorithm reduces high variance and over-fitting associated with the individual regression trees, and thereby, improves the predictive accuracy of the surrogate model. For the present study we use *scikit-learn* [50] which is a Python module that integrates several state-of-the-art machine learning algorithms. The main steps involved in the RF algorithm are shown in Fig.2.

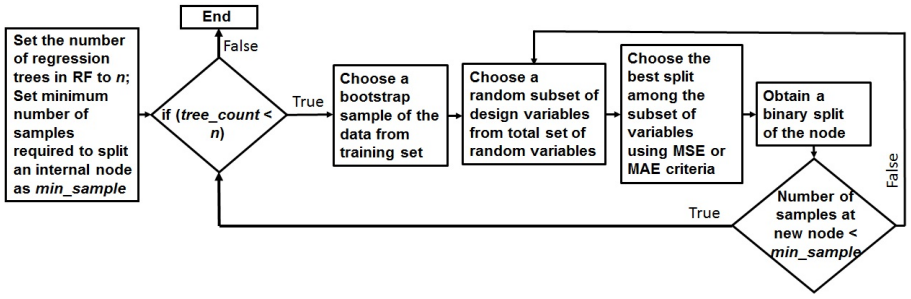

Figure 2: Algorithm for training Random Forest model

3.2. Polynomial chaos expansion.

The idea behind PCE is to project the stochastic output $y(\boldsymbol{\xi})$ in the n-dimensional random space spanned by orthogonal polynomial basis $\psi(\boldsymbol{\xi})$ which are functions of the n-dimensional random variable $\boldsymbol{\xi} = \{\xi_1, \xi_2, \ldots, \xi_n\}$. The output function, which can be displacement, stress or modal characteristics like natural frequency, can be expanded using PCE as shown in Eq.(15)

$$y(\boldsymbol{\xi}) = \sum_{i=0}^{\infty} c_i \psi_i(\boldsymbol{\xi}) \approx \sum_{i=0}^{P} c_i \psi_i(\boldsymbol{\xi}) \tag{15}$$

where, c_i are unknown coefficients in the expansion that need to be evaluated. For practical reasons, the series is truncated by limiting the order of basis polynomials, p. The orthogonality of the basis functions with respect to the probability distribution of the random variables implies that the inner product of the function satisfy Eq.(16)

$$\langle \psi_r(\boldsymbol{\xi}), \psi_s(\boldsymbol{\xi}) \rangle = \int_{\Omega} \psi_r(\boldsymbol{\xi}) \psi_s(\boldsymbol{\xi}) d\mu(\boldsymbol{\xi}) = \gamma_n \delta_{rs} \tag{16}$$

where, γ_n are constants, δ_{rs} is the Kronecker delta and $d\mu(\boldsymbol{\xi})$ is the probability measure in the n-dimensional random space given by Eq.(17) for statistically independent random variables

$$d\mu(\boldsymbol{\xi}) = \rho_1(\xi_1)\rho_2(\xi_2)\dots\rho_n(\xi_n)d\xi_1 d\xi_2 \dots d\xi_n \tag{17}$$

where, ρ_n is the probability density function of ξ_n. The choice of basis functions in Eq.(15) is based on the probability distribution of the random variables. For the case of the univariate output function, Table 1 provides examples of basis functions for some common random distributions: (i) normal distribution, (ii) uniform distribution and (iii) exponential distribution: $\rho = \lambda e^{-\lambda \xi}$. For conciseness, the basis functions are provided here for special values of the parameters of the statistical distributions: (i) mean value, $\mu = 0$ and STD, $\sigma = 1$ - for normal distribution; (ii) uniform distribution is taken over interval $[-1, 1]$; $\lambda = 1$ is assumed for exponential distribution. The basis function expressions can be obtained for any realistic parameter values of these and many other distributions. For the case of multivariate output functions, the polynomial basis functions are obtained as tensor products of the orthogonal polynomial basis for corresponding univariate cases.

Table 1: Choice of basis functions

Distribution	Polynomial	Basis functions
Normal $(\mu = 0, \sigma = 1)$	Hermite	$\psi_0 = 1, \psi_1 = \xi,$ $\psi_2 = (\xi^2 - 1)/\sqrt{2}, \dots$
Uniform $(-1, 1)$	Legendre	$\psi_0 = 1, \psi_1 = \sqrt{3}\xi,$ $\psi_2 = \sqrt{5}(3\xi^2 - 1)/2, \dots$
Exponential $(\lambda = 1)$	Laguerre	$\psi_0 = 1, \psi_1 = \xi - 1,$ $\psi_2 = (\xi^2 - 4\xi + 2)/2, \dots$

When the number of evaluations of the exact model is greater than the number of coefficients in Eq.(15), then the system of linear equations is overdetermined and is solved using the least squares approach.

3.3. Polynomial chaos expansion using gradient information.

The number of terms in the PCE increases exponentially as the dimension of random space increases, increasing the computational cost. This problem is often referred to in the literature as the "curse of dimensionality". To address this issue, the use of gradient values in evaluating the coefficients of polynomial response surfaces for maximum amplitude of vibrations in mistuned bladed disks was shown to be very useful (see Ref. [51], [52]). For an n-dimensional random

space, the number of linearly independent equations obtained by including gradient values is $(1+n)$ times the number of FE evaluations where n is the number of random variables. Therefore, the minimum number of model evaluations required to obtain the coefficients in a polynomial approximation is reduced by a factor of $1/(1+n)$. In addition to the value of the output function, the values of the gradients of the output function with respect to random design parameters evaluated at chosen points are used to determine the coefficients of PCE:

$$\begin{bmatrix} \psi_0(\boldsymbol{\xi}_1) & \psi_1(\boldsymbol{\xi}_1)\dots\psi_P(\boldsymbol{\xi}_1) \\ \frac{\partial\psi_0(\boldsymbol{\xi}_1)}{\partial\xi_1} & \frac{\partial\psi_1(\boldsymbol{\xi}_1)}{\partial\xi_1}\cdots\frac{\partial\psi_P(\boldsymbol{\xi}_1)}{\partial\xi_1} \\ \vdots & \\ \frac{\partial\psi_0(\boldsymbol{\xi}_1)}{\partial\xi_n} & \frac{\partial\psi_1(\boldsymbol{\xi}_1)}{\partial\xi_n}\cdots\frac{\partial\psi_P(\boldsymbol{\xi}_1)}{\partial\xi_n} \\ \vdots & \\ \psi_0(\boldsymbol{\xi}_N) & \psi_1(\boldsymbol{\xi}_N)\dots\psi_P(\boldsymbol{\xi}_N) \\ \vdots & \\ \frac{\partial\psi_0(\boldsymbol{\xi}_N)}{\partial\xi_n} & \frac{\partial\psi_1(\boldsymbol{\xi}_N)}{\partial\xi_n}\cdots\frac{\partial\psi_P(\boldsymbol{\xi}_N)}{\partial\xi_n} \end{bmatrix} \cdot \begin{Bmatrix} c_0 \\ c_1 \\ \vdots \\ c_P \end{Bmatrix} = \begin{Bmatrix} y(\boldsymbol{\xi}_1) \\ \frac{\partial y(\boldsymbol{\xi}_1)}{\partial\xi_1} \\ \vdots \\ \frac{\partial y(\boldsymbol{\xi}_1)}{\partial\xi_n} \\ \vdots \\ y(\boldsymbol{\xi}_N) \\ \vdots \\ \frac{\partial y(\boldsymbol{\xi}_N)}{\partial\xi_n} \end{Bmatrix} \tag{18}$$

where, $\psi_0(\boldsymbol{\xi}_1)$, $\psi_1(\boldsymbol{\xi}_1)$, ..., $\psi_P(\boldsymbol{\xi}_1)$ are basis functions evaluated at the first sample point, c_0, c_1, ..., c_P are deterministic coefficients in the polynomial expansion, and $y(\boldsymbol{\xi}_1)$, ..., $y(\boldsymbol{\xi}_N)$ are exact values of the output obtained from N number of FE model evaluations. $\partial y(\boldsymbol{\xi}_i)/\partial\xi_j$ represents the gradient value of output with respect to the j^{th} random parameter evaluated for the i^{th} model evaluation.

4. Global Sensitivity Analysis

Sobol indices is a measure of sensitivity based on the variance decomposition method which allows partitioning of the output variance into contributions from each of the input parameters. It is classified as a global sensitivity measure which differs from the gradient-based local sensitivity analysis in its ability to account for the variation in design parameters over its entire domain of variation. On the other hand, the local sensitivity analysis is based on an evaluation of gradients at any chosen point in the domain of variation of the design parameters.

The analysis of variance representation allows decomposition of stochastic output $f(\boldsymbol{\xi})$ into summands of increasing dimensions as it was shown in Ref. [45]:

$$y = f(\boldsymbol{\xi}) = f_0 + \sum_{i=1}^{n} f_i(\xi_i) + \sum_{1\le i<j\le n} f_{i,j}(\xi_i,\xi_j) + \cdots + f_{1,\dots,n}(\xi_1,\dots,\xi_n) \tag{19}$$

where n is the total number of random input parameters.

This allows the decomposition of the variance of y to be written in the form:

$$D = \sum_{i=1}^{n} D_i + \sum_{1\le i<j\le n} D_{ij} + \cdots + \sum_{1\le i_1<\cdots<i_s\le n} D_{i_1,\dots,i_s} + \cdots + D_{1,2,\dots,n} \tag{20}$$

where, $D_i = \text{var}(\mathbb{E}[y|\xi_i])$ is the first order partial variance; $D_{ij} = \text{var}(\mathbb{E}[y|\xi_i, \xi_j]) - D_i - D_j$ is the second-order partial variance, and so on, and

$$D_{i_1,\ldots,i_s} = \int_{\Omega_{\boldsymbol{\xi}_k}} f^2_{i_1,\ldots,i_s}(\boldsymbol{\xi}_k) \prod_{j=1}^{s} \rho_{i_j}(\xi_{i_j}) \mathrm{d}\xi_{i_j} \;\; \forall \;\; k = \{i_1, \ldots, i_s\} \tag{21}$$

The first order partial variance, D_i, can be understood as the average reduction in the variance of y when the value of ξ_i is fixed. Therefore, the first order partial variance with respect to an input parameter gives the individual contribution of that parameter to the output variance. The second-order partial variance D_{ij} measures the contribution to the output variance due to the interaction between ξ_i and ξ_j.

The Sobol sensitivity indices are obtained by dividing the partial variance by the total variance D:

$$S_{i_1,\ldots,i_s} = \frac{D_{i_1,\ldots,i_s}}{D} \tag{22}$$

$S_{i_1,\ldots,i_s}$ is a measure of the contribution to the total variance coming from the uncertainty in set of design parameters $\{\xi_{i_1}, \ldots, \xi_{i_s}\}$.

From eqn.(20) and eqn.(22), the sensitivity indices satisfy the condition

$$\sum_{i=1}^{n} S_i + \sum_{1 \le i < j \le n} S_{ij} + \cdots + S_{1,2,\ldots,n} = 1 \tag{23}$$

The total order Sobol indices S_i^{tot} are defined as the sum of all Sobol indices, starting from first order to the maximum order, that involve the input parameter i. For example for $n = 3$, the total order Sobol index for the first parameter is

$$S_1^{tot} = S_1 + S_{12} + S_{13} + S_{123} = 1 - S_2 - S_3 \tag{24}$$

The total order Sobol indices can be used to rank the parameters in the order of their importance in contributing to the variance of output $y(\xi)$. Considering the extreme cases: (i) when $S_i^{tot} = 0$: it means that the uncertainty in parameter i does not contribute to the uncertainty in the system response and (ii) when $S_i^{tot} = 1$: it implies that the uncertainty in output is solely due to the uncertainty in parameter i.

The conventional method for calculating Sobol indices using MCS is computationally intensive. Polynomial chaos based calculation of Sobol indices was proposed as an alternative to using MCS in Ref. [46].

5. Numerical studies of bladed disk models

The methodology described in previous sections for uncertainty and global sensitivity analysis using surrogate models is applied to a realistic bladed disk model. The full model of the bladed disk is shown in Fig.1a. The blades are attached to the disk using fir tree root joints and the adjacent blades are also connected through shrouds. For the analysis of tuned bladed disk, the sector model (shown in the inset in Fig. 1a) of the bladed disk is used. In the analysis presented in this study, the authors have not considered the variation material properties due to variation in temperature.

To study the effect of variations in root geometry on the static deformation, bladed disk sector models with different root geometries are studied. Five different root geometry variants, each differing in the relative position of contact surfaces on the fir tree, are chosen for the study. Nominal geometry (Fig. 3a) has contacts on upper and lower surfaces on both sides of the fir tree. The variant "Lower" (Fig. 3c) has contact only at lower fir tree surfaces prior to applying load and the variant "Upper" (Fig. 3b) has contact only at upper fir tree surfaces. The variants "Asym-A" (Fig. 3d) and "Asym-B" (Fig. 3e) have asymmetric contact geometries with each side of the blade having contact surfaces either on the upper fir tree or lower fir tree as shown in the figure.

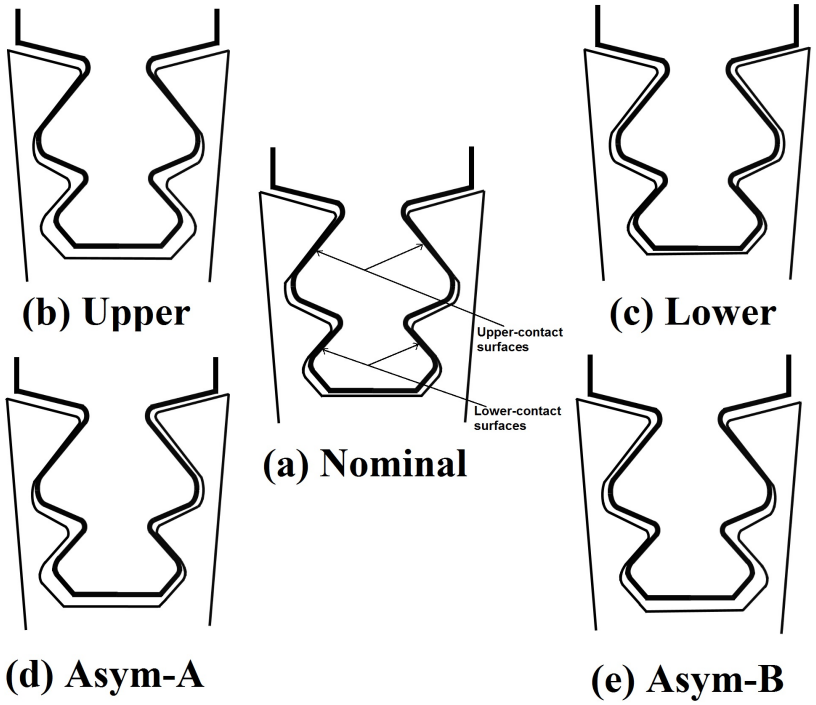

Figure 3: Variants of fir tree root geometry.

5.1. Bladed disk models

The FE models for full bladed disk and sector model are shown in Fig. 4(a) and (b) respectively. The total number of blades in the bladed disk is 75. The disk is modelled as isotropic material and the blades are modelled as an anisotropic material. For the tuned bladed disk case, a sector model of the bladed disk is analyzed with cyclic symmetric constraints applied on all nodes on either side of the sector model. Ten node tetrahedral elements are used to model the blade and disk and have 126275 nodes. Face to face penalty frictional contact elements are used to define the contacts. The frictional and unilateral interactions are considered at (i) blade–disk interfaces and (ii) at shrouds in the blade sector model. The axial and tangential degrees of freedom for nodes on the rim of the disk is constrained.

The FE mesh for the full bladed disk model used for the analysis of the mis-

tuned case has 0.5 million nodes. Similar to that for the sector model, face-to-face penalty frictional contact elements are used to define the contacts at root and shroud contact interfaces. The total number of friction contact elements in the FE model of the full bladed disk is 17475. The FE analysis is performed using *CalculiX* [53], which is an open source FE analysis package. The capability for sensitivity analysis with respect to material anisotropy orientation was introduced in *CalculiX* as part of the current project (see [54]).

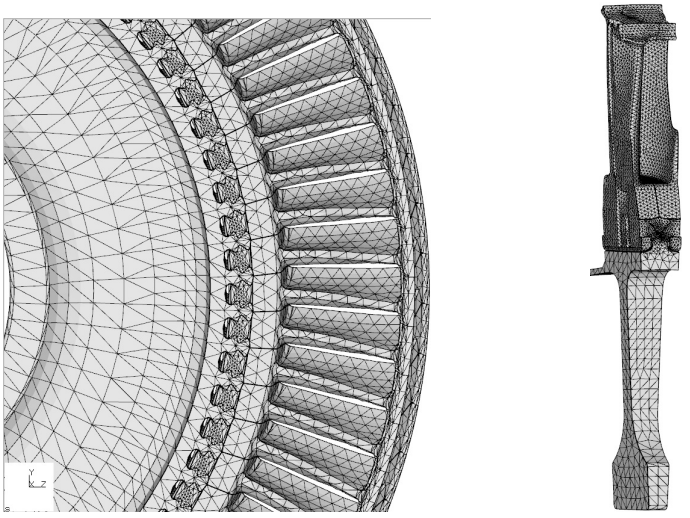

(a) (b)

Figure 4: FE mesh of (a) full bladed disk and (b) blade sector model.

5.2. Tuned bladed disks

The effects of scattering in anisotropy angles on the deformation of tuned bladed disks for the following cases of fir tree root contact geometry variation are investigated (i) Nominal, (ii) Upper, (iii) Lower, (iv) Asym-A, and (v) Asym-B. In the present study the effects of crystal orientation on static displacements of the blades and the contact pressure at fir tree roots are investigated. For any root geometry variant of bladed disk, the contact stresses experienced by fir tree roots under centrifugal loading is directly proportional to the contact pressure on the surface for that geometry. The average value of contact pressure on a fir tree root surface is calculated as the mean value of contact pressure on all finite element nodes on that surface.

5.2.1. Effects of root geometry.

To study the effects of root geometry on the deformation of bladed disks under centrifugal force, blade sector models with five different root geometry conditions have been investigated. Fig. 5 shows an example of the radial displacement of blades with the Nominal geometry and Asym-A contact geometry. The figure shows that there is a noticeable difference in displacements near the blade tip region. For the cases studied, Table 2 shows the values of maximum blade displacements in radial, tangential and axial direction along with the values for resultant displacements. The values for displacement are normalized with

respect to the corresponding value for nominal geometry. From the table, it is clear that a maximum deviation of 8.2%, 66.4% and 13.9% is possible for displacements in radial, tangential and axial direction respectively.

Table 2: Variation in normalised maximum blade displacements

Root geometry variants	Normalised maximum blade displacements			
	Radial	Tangential	Axial	Resultant
Nominal	1.000	0.398	0.623	1.205
Upper	1.023	0.431	0.598	1.202
Lower	1.045	0.546	0.648	1.288
Asym-A	1.004	0.157	0.686	1.174
Asym-B	1.094	0.656	0.648	1.374

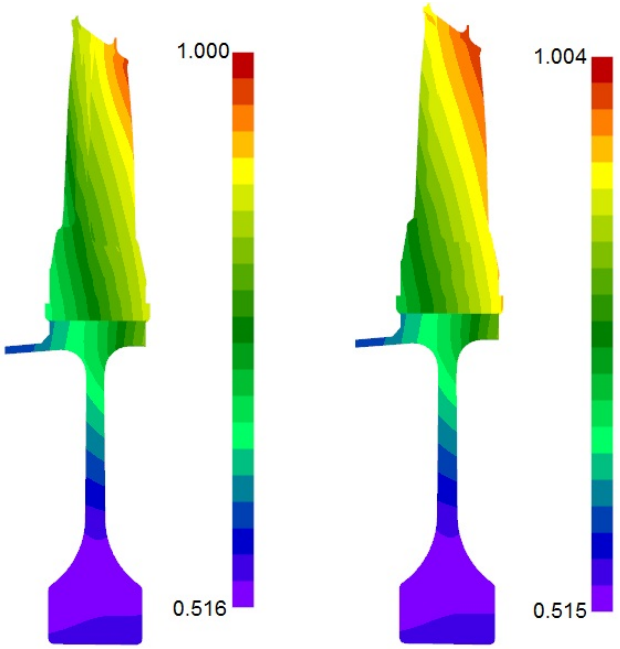

(a) (b)

Figure 5: Radial displacement of blade sector for cases: (a) Nominal, (b) Asym-A

5.2.2. Effects of anisotropy axis orientation.
To study the effects of variation in primary anisotropy angle α on blade deformations, keeping the values of anisotropy angles β and ζ constant, the value of α was increased. Table 3 gives the variation in average contact pressure for left side of the fir tree as the value of one of the anisotropy angles, α, is increased from X to $9X$ in steps of $2X$, keeping the other two angles as constant. The values are normalized with respect to to the corresponding values on upper-left fir tree surface for Nominal geometry when blade anisotropy axis is aligned with blade geometric axis. Note that while the variation in contact pressure is negligible for the three symmetric root geometry variants including

the nominal geometry, for asymmetric root geometry cases the contact pressure has noticeable variation with respect to angle α.

Table 3: Variation in average contact pressure with respect to anisotropy angle α

Root geometry variants	Normalised average contact pressure				
	Left side of fir tree				
	X	$3 \times X$	$5 \times X$	$7 \times X$	$9 \times X$
Asym-A	2.07	2.03	2.01	1.96	1.97
Asym-B	2.52	2.52	2.51	2.52	2.50
Lower	2.15	2.15	2.15	2.14	2.15
Nominal	1.51	1.52	1.53	1.54	1.54
Upper	1.12	1.12	1.12	1.12	1.13

5.2.3. Uncertainty analysis.
To efficiently calculate the statistical characteristics for blade deformation with respect to variations in root geometry and anisotropy orientation, the RF-based surrogate model is used. The input parameters for this model will include four categorical variables and three continuous variables. The categorical variables are used to determine whether the blade root surfaces are in contact or out of contact with corresponding disk surfaces, the continuous variables are the three anisotropy angles. The probability distribution function for the anisotropy angles was provided by the manufacturer of the single blades.

To build the RF-based surrogate model, for each of the five root geometry variants, FE model evaluations are obtained based on sampling of anisotropy angles α, β and ζ using Sobol sequences from the known probability distribution for these angles. The blade deformation values obtained from model evaluations are divided into the training set and test set in the proportion 9:1. The choice of the ratio of the training set to test set is made such that most of the function evaluations obtained from FE analysis are used for building the RF model. From Table 3 it is evident that the variation in average contact pressure is significant for the two models with asymmetric root contact geometry compared to that for the other three geometry variants studied. Therefore, to minimize the computational cost associated with building the RF model, 20 FE model evaluations of Nominal, Upper and Lower geometry models each and 60 FE model evaluations of Asym-A and Asym-B models each are used.

The residual error in predicted values for the normalized average contact pressure on the left side contact surface is shown in Fig. 6. The residual error is calculated as the difference between the predicted value and the true value obtained using model realization. The values of predicted average contact pressure and the corresponding residual are normalized with respect to the value of average contact pressure for the Nominal geometry. The maximum error in prediction is less than 6.5% of the predicted value of contact pressure for all root geometry variants analyzed. The figure shows that the predicted values for contact pressure form clusters where each of the clusters corresponds to a different root geometry variant.

The accuracy of the surrogate models can be expressed in terms of normalized mean squared error which is defined as the ratio of the difference in the variance

of predicted value from mean squared error to variance of the predicted value:

$$R^2 = (Var(y) - MSE(y))/Var(y) \tag{25}$$

where, $Var(y) = \sum_{i=1}^{n}(y^{(i)} - \bar{y})^2/n$; $\bar{y}$ being the mean of the predicted value, $y^{(i)}$ the i^{th} predicted value and $MSE(y)$ is the mean square error of the RF prediction. For the case when $R^2 = 1$, the model captures the variation in the response variable perfectly. For the present RF model, the R^2 values for the training set and test set are shown in Table 4. The error estimate indicates that the RF model can sufficiently capture the variation in average contact pressure at the fir tree root joints with respect to variation in the root geometry and blade material anisotropy angles.

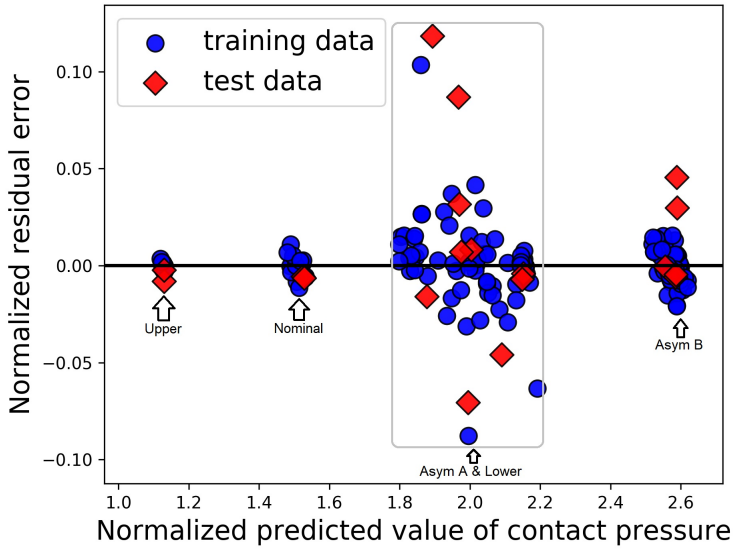

Figure 6: Residual error in prediction of normalized average contact pressure.

Table 4: Accuracy estimate for RF model

Contact surface	R^2 value	
	Training set	Test set
Left side	0.999	0.991
Right side	0.999	0.992

For Monte Carlo simulations using the FE model and an RF-based surrogate model, the convergence of the mean and STD of average contact pressure on the left side of the fir tree root joint for Asym-B variant is shown in Fig.7. While the mean value of average contact pressure obtained using the surrogate model converges to that obtained using the FE model based Monte Carlo simulation, there is a noticeable difference in the converged value of the STD obtained from the two models. It must be noticed from the figure that the convergence in

statistical characteristics obtained from the RF-based model is faster, especially for the mean value, compared to that obtained using the FE model.

The normalized mean and the STD for average contact pressure with respect to variation in the anisotropy angles are calculated for different root geometry variants using the RF model. The statistics are calculated from one thousand random samples of the blade anisotropy angles as the computational cost associated with RF model evaluation is negligible. Table 5 gives the value of the mean and STD for average contact pressure on the left and right side fir tree for different root geometry variants. The mean values of average contact pressure for each variant are normalized with respect to the corresponding value for the upper-left surface of the fir tree for Nominal geometry with the crystal axis aligned with the geometry axis. As indicated by the value of STD, the variation in average contact pressure is significant for the two geometries with asymmetric contacts. This indicates that for the two geometries with asymmetric contacts the effect of uncertainty in the crystal orientation results in comparatively high uncertainty in average contact pressure values at the fir tree root interfaces.

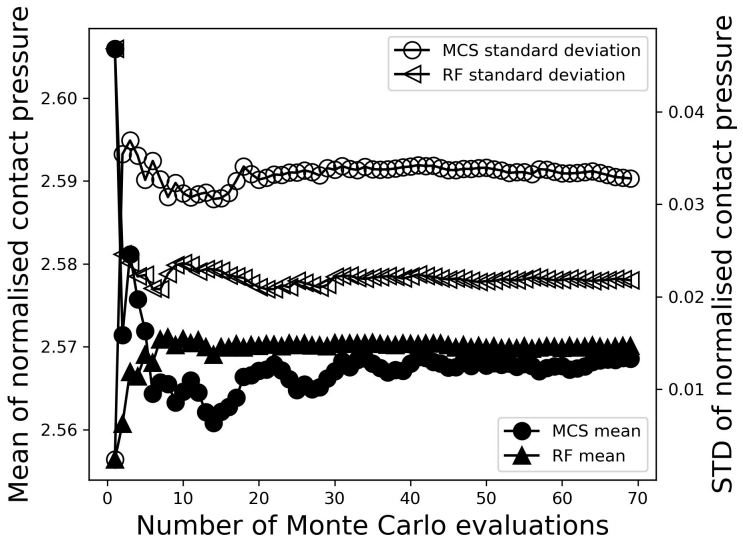

Figure 7: Convergence of normalized mean and STD of average contact pressure on left side of fir tree for Asym-B variant.

5.3. Mistuned bladed disks

5.3.1. Uncertainty analysis.

The effects of mistuning due to the material anisotropy orientation on static deformation of the bladed disks with nominal root geometry are investigated in this section. For efficient estimation of the scattering in blade displacements due to random blade anisotropy orientation, PCE-based surrogate models are used. The statistics for blade displacements of a mistuned bladed disk are calculated using the gradient-enhanced PCE (gradPCE) surrogate model of second-order. For mistuned bladed disks with linear contacts, it has been shown that the value of mean and STD obtained using second-order gradPCE will converge to the

Table 5: Statistics of normalised average contact pressure on fir–tree contact surfaces

Root geometry variant	Statistical characteristics							
	Left Side				Right Side			
	Mean		STD		Mean		STD	
	RF	MCS	RF	MCS	RF	MCS	RF	MCS
Asym-A	1.960	1.964	0.086	0.095	2.689	2.685	0.061	0.064
Asym-B	2.571	2.568	0.030	0.0325	1.740	1.732	0.062	0.079
Nominal	1.509	1.513	0.012	0.016	1.480	1.479	0.006	0.008
Upper	1.125	1.127	0.004	0.005	1.307	1.306	0.010	0.013
Lower	2.072	2.061	0.006	0.008	2.150	2.149	0.006	0.008

Monte-Carlo estimates with fewer model evaluations compared to conventional PCE [37]. In Ref. [37], the reduction in computational cost obtained by using gradient enhanced PCE in comparison with conventional PCE method has been presented. In this paper, global sensitivity analysis for blade displacements with respect to uncertainty in blade anisotropy orientations of a mistuned bladed disk is presented.

Using gradPCE, the statistics for blade#1, displacements for the following two cases are calculated (i) 9 (Fig.9a) and (ii) 30 (Fig.9b) blades adjacent to the considered blade have random anisotropy orientations. For the first case, a comparison of statistics obtained from two different approaches for sampling namely Sobol sequences [55] and pseudo-random sampling is presented. Further, global sensitivity analysis for blade displacements with respect to variation in blade anisotropy orientations was performed. The present study uses *Chaospy* [56] to obtain PC based statistics and to obtain Sobol indices.

For the example case of a mistuned bladed disk, the radial displacement (Fig. 8) shows small differences from blade to blade. This is not discernible from the plot of displacements for the full bladed disk. In order to highlight the scatter in radial displacements, a zoomed view of several blades in the bladed disk is shown in the inset. To estimate the maximum possible range in the scattering of blade displacements, 250 different mistuning patterns of blade anisotropy orientations are studied. Considering the displacements at blade tip node of all 75 blades in the bladed disk, across 250 mistuning patterns, maximum percentage scatter in displacement is calculated. Table 6 shows that a maximum scatter of 16.7%, 18.6% and 3.0% is possible in axial, tangential and radial direction respectively. The blade tip displacement values in axial, circumferential and radial direction are normalized with respect to corresponding values for the tuned bladed disk where the blade anisotropy angles of all blades are aligned with blade geometry axis.

To obtain PCE approximations for blade displacements, the coefficients in the PC expansion must be calculated using FE model evaluations. There are different approaches to sample the input parameter space. Table 7 shows the statistics for normalized displacements at blade#1 tip, with respect to variation in anisotropy angles of 9 blades, obtained using two different sampling approaches. It is evident that for the present study, the choice of sampling approach has a negligible effect on the statistical characteristics obtained. The variations in displacements are small, especially in the radial direction as indicated by the

value of STD. To capture the effect of randomness in anisotropy orientation of more blades, the polynomial chaos approximation was expanded by including anisotropy angles of 30 blades (Fig.9b) as random variables. Table 8 shows that the value of mean and STD for normalized blade#1 tip displacements have not increased even though the number of blades in the bladed disk with random anisotropy angles was increased from 9 to 30.

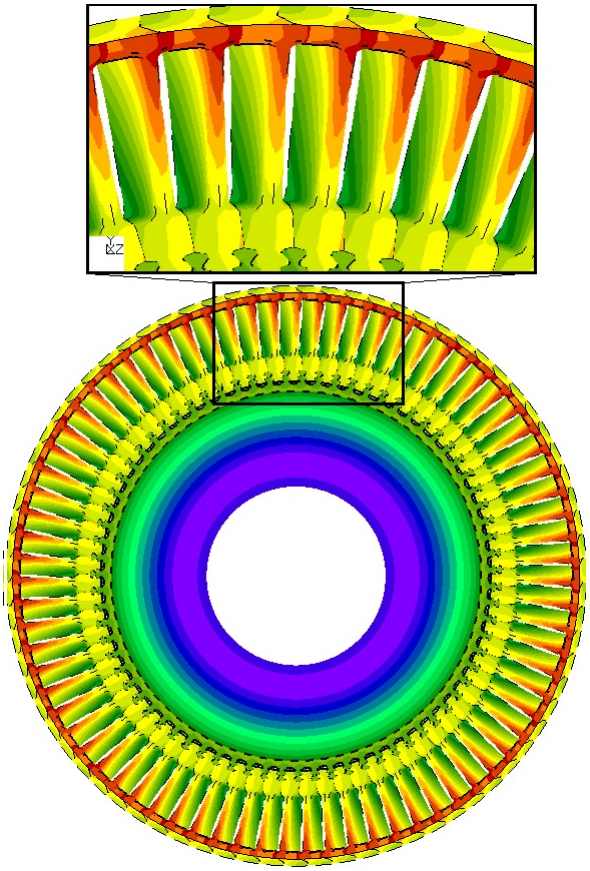

Figure 8: Radial displacement of mistuned bladed disk

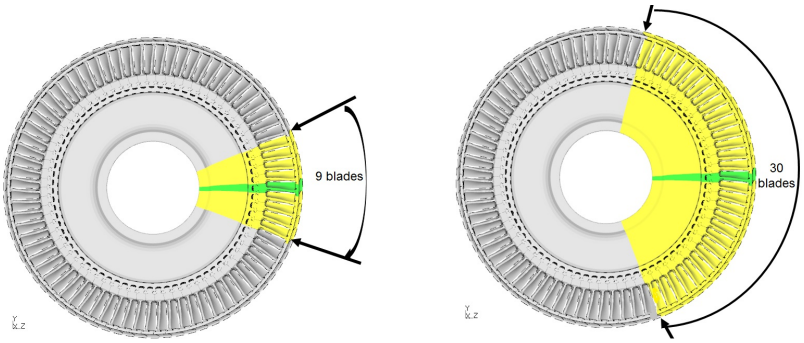

(a) (b)

Figure 9: Mistuned bladed disk with (a) 9 and (b) 30 blades having random anisotropy angles.

Table 6: Scatter in normalized blade tip displacements

Displacement component		Displacement	Maximum scatter (%)
Axial	Max.	1.0972	16.7
	Min.	0.9273	
Circumferential	Max.	1.0459	18.6
	Min.	0.8674	
Radial	Max.	1.0045	3.0
	Min.	0.9744	

Table 7: Statistics for normalized blade tip displacements obtained from gradient based PCE

Type of sampling	Displacement	Mean	STD
Sobol sequence	Axial	1.0034	0.0347
	Tangential	0.9809	0.0373
	Radial	0.9936	0.0056
Psuedo-random	Axial	1.0053	0.0355
	Tangential	0.9779	0.0367
	Radial	0.9927	0.0061

Table 8: Statistics for normalized blade tip displacements

Number of of random blade angles	Number of terms in PCE	Model evaluations	Displacement	Mean	STD
27	406	110	Axial	1.0042	0.0345
			Tang.	0.9797	0.0363
			Rad.	0.9924	0.0059
90	4186	110	Axial	1.0040	0.0309
			Tang.	0.9787	0.0300
			Rad.	0.9924	0.0059

5.4. Global sensitivity analysis

Global sensitivity analysis is performed to understand the effect of individual blade anisotropy angles of bladed disks on displacements at blade#1 tip. A quantitative measure for the influence of each blade anisotropy angle on the static displacement of blade#1 is obtained by calculating Sobol indices for blade displacements. Figure 10(a) & (b) shows the Sobol indices for axial displacement on blade#1 tip with respect to variation in anisotropy angles α and ζ of 30 adjacent blades respectively. As described in section 4, while the first order index is a measure of the contribution to displacement variance due to the randomness of individual blade anisotropy angles considered alone, total order index also accounts for the possible contribution to output variance due to the interaction of an angle with other anisotropy angles. Therefore, the total order index of a blade anisotropy angle is always greater than its first order index. For a given anisotropy angle, the difference between total order index and first order index is a measure of the contribution to blade displacement variance resulting from the interaction between the angle with other anisotropy angles. It is evident from Figure 10(b), that more than 50% of the variance in axial displacement of blade#1 is due to anisotropy angle ζ of blade#1 and blade#75. In the same figure, the small difference in magnitude of first order index from total order index for blade#1 confirms that the uncertainty in anisotropy angle ζ of blade#1 has a predominant effect on uncertainty of axial displacement on that blade. Figure 10(a) shows that the contribution to axial displacement variance of blade#1 from anisotropy angle α of that blade#1 is mostly due to the interaction of the angle with other anisotropy angles. The uncertainty in the value of anisotropy angle β of blades contributes only marginally to uncertainty in axial displacement of blade#1 as indicated by Sobol indices for that angle which is not shown here for the sake of brevity. From Fig. 11(a) & (b) it is clear that the most predominant effect on the variance of radial displacement of blade#1 is due to scattering in anisotropy angles α followed by ζ. Finally, from the value of Sobol indices, it is apparent that the randomness in anisotropy angles of blades located farther from blade#1 has a negligible effect on the uncertainty in displacements on blade#1. Therefore, accounting for uncertainty in anisotropy angles of more number of blades farther from blade#1 will not increase the scatter in static displacements of blade#1.

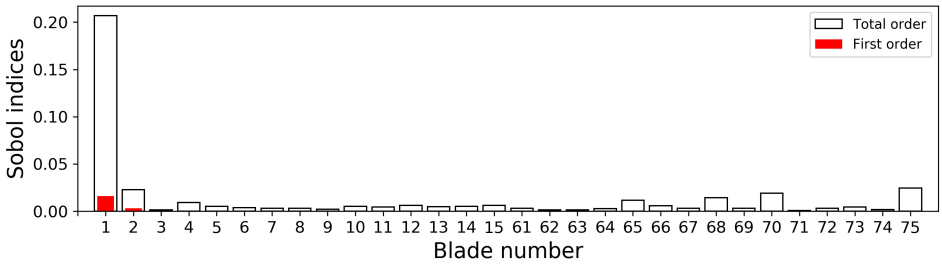

(a)

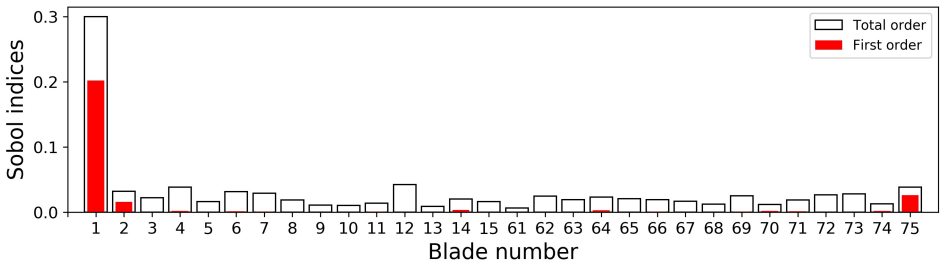

(b)

Figure 10: Sobol index for axial displacement at blade#1 w.r.t angle (a) α and (b) ζ.

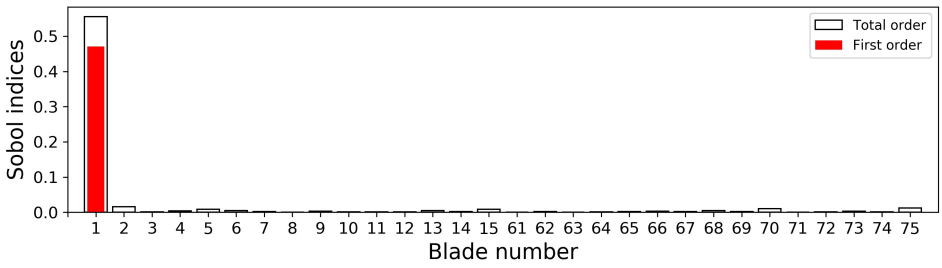

(a)

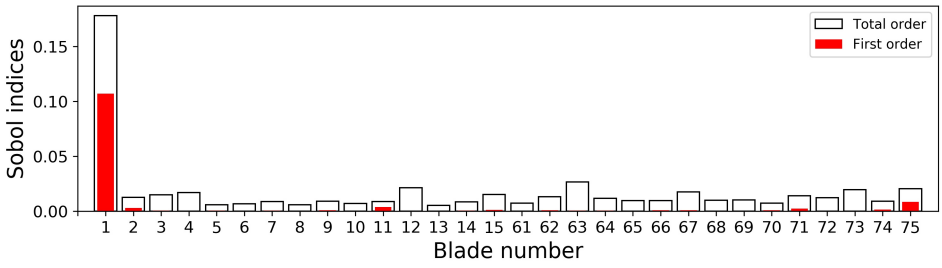

(b)

Figure 11: Sobol index for radial displacement at blade#1 w.r.t angle (a) α and (b) ζ.

6. Conclusions

For efficient uncertainty analysis of deformation of high-fidelity bladed disk models, the usefulness of surrogate models based on random forest and polynomial chaos expansion has been studied. For mistuned bladed disks with numerous random parameters, in the form of blade anisotropy angles, gradient enhanced polynomial chaos expansion has been used to reduce the computational cost involved in building PCE approximation.

The effect of variations in blade material anisotropy orientations on the deformation of bladed disks with friction contacts at fir tree root and shroud has been investigated. For tuned bladed disk under static centrifugal load, the effect of variation in anisotropy orientation on blade displacements has been investigated taking into consideration some of the possible variations in fir tree root geometry. It has been observed that for root geometry variants with asymmetric contacts on fir tree root, the influence of anisotropy orientation is noticeable compared to that for nominal design geometry. The usefulness of the random forest surrogate model in performing uncertainty analysis for the static deformation of bladed disk has been investigated. Statistics for contact pressure at fir tree root joint obtained through numerous Monte Carlo evaluations of RF model has been compared with that obtained using the FE model. For some root geometry variants, faster convergence for mean and STD of contact pressure has been obtained from the RF model compared to that obtained using the FE model based MCS. For those models, this has resulted in a reduction in computational cost involved in uncertainty analysis when using the surrogate model.

For bladed disks with material anisotropy mistuning, analysis has been performed to quantify the uncertainty in blade displacements due to scattering in anisotropy angles of several blades. Gradient enhanced polynomial chaos expansion has been used to calculate the statistical characteristics for blade displacements efficiently. Using PCE, Sobol indices for blade displacements with respect to variation in anisotropy angles of individual blades in the bladed disk has been obtained. It has been inferred that the scatter in displacements of a blade in a bladed disk is predominantly due to the scatter in anisotropy angles of that blade and to some degree due to the interaction of the anisotropy angles of the blade with anisotropy angles of rest of the blades in the bladed disk.

7. Acknowledgements

The authors are grateful to MTU Aero Engines AG, Germany for the financial and technical support provided for the current project. The first author is grateful to MTU Aero Engines AG for their sponsorship of his doctoral study at Sussex University through MTU Scholarship.

References

[1] M. Segersäll, D. Leidermark, J. J. Moverare, Influence of crystal orientation on the thermomechanical fatigue behaviour in a single-crystal superalloy, Materials Science and Engineering: A 623 (2015) 68–77.

[2] Y. Kaneko, Study on vibration characteristics of single crystal blade and directionally solidified blade, in: *Proc. of the ASME Turbo Expo*. GT2011-45032. Vancouver, Canada, June 6-10, 2011.

[3] M. Manetti, I. Giovannetti, N. Pieroni, H. Horculescu, G. Peano, G. Zonfrillo, M. Giannozzi, The dynamic influence of crystal orientation on a second generation single crystal material for turbine buckets, in: *Proc. of the ASME Turbo Expo*. GT2009-59091. Orlando, Florida, USA, June 8–12, 2009.

[4] Z. Wen, H. Mao, Z. Yue, B. Wang, The influence of crystal orientation on vibration characteristics of dd6 nickel-base single crystal superalloy turbine blade, J. of Materials Engineering and Performance 23 (2) (2014) 372–377.

[5] M. W. R. Savage, The influence of crystal orientation on the elastic stresses of a single crystal nickel-based turbine blade, in: *Proceedings of the ASME Turbo Expo*. GT2011-45309. Vancouver, Canada, June 6-10, 2011.

[6] N. Arakere, G. Swanson, Effect of crystal orientation on fatigue failure of single crystal nickel base turbine blade superalloys, Journal of Engineering for Gas Turbines and Power 124 (1) (2002) 161–176.

[7] T. Weiss, M. Voigt, H. Schlums, R. Mücke, K.-H. Becker, K. Vogeler, Probabilistic finite-element analyses on turbine blades, in: *Proc. of the ASME Turbo Expo*. GT2009-59877. Orlando, Florida, USA, June 8–12, 2009.

[8] S. A. Meguid, P. S. Kanth, A. Czekanski, Finite element analysis of fir-tree region in turbine discs, Finite Elements in Analysis and Design 35 (4) (2000) 305 – 317.

[9] S. Meguid, M. Refaat, P. Papanikos, Theoretical and experimental studies of structural integrity of dovetail joints in aeroengine discs, Journal of Materials Processing Technology 56 (1996) 668–677.

[10] G. B. Sinclair, N. G. Cormier, J. H. Griffin, G. Meda, Contact stresses in dovetail attachments: Finite element modeling, J. of Engineering for Gas Turbines and Power 124 (1) (2002) 182–189.

[11] L. Witek, Failure analysis of turbine disc of an aero engine, Engineering Failure Analysis 13 (1) (2006) 9–17.

[12] C. Sun, Y. Zhou, J. Chen, H. Miao, Measurement of deformation close to contact interface using digital image correlation and image segmentation, Experimental Mechanics 55 (8) (2015) 1525–1536.

[13] M. Gean, T. Farris, Finite element analysis of the mechanics of blade/disk contacts, in: 46th AIAA/ASME/ASCE/AHS/ASC Structures, Structural Dynamics and Materials Conference, American Institute of Aeronautics and Astronautics, AIAA2005-1907, 2005.

[14] J. R. Beisheim, G. B. Sinclair, On the three-dimensional finite element analysis of dovetail attachments, Journal of Turbomachinery 125 (2) (2003) 372–379.

[15] J. R. Beisheim, G. B. Sinclair, Three-dimensional finite element analysis of dovetail attachments with and without crowning, Journal of Turbomachinery 130 (2) (2008) 021012.

[16] F. Wagner, A. Kühhorn, T. Weiss, D. Otto, Influence of different parametrizations on the optimum design of a high pressure turbine blade firtree, in: *Proc. of the ASME Turbo Expo*. GT2016-56749. Seoul, South Korea, June 13-17, 2016.

[17] D. Yu, F. Li, J. Yang, K. Cheng, W. Shu, K. Lv, M. Li, Structural optimization of fir-tree root and groove for turbine blade with splines and genetic algorithm, in: *Proc. of the ASME Turbo Expo*. GT2016-56518. Seoul, South Korea, June 13-17, 2016.

[18] W. Song, A. Keane, J. Rees, A. Bhaskar, S. Bagnall, Turbine blade fir-tree root design optimisation using intelligent cad and finite element analysis, Computers & Structures 80 (24) (2002) 1853–1867.

[19] W. Song, A. Keane, J. Rees, A. Bhaskar, S. Bagnall, Local shape optimisation of turbine disc firtrees using nurbs, in: 9th AIAA/ISSMO Symposium on Multidisciplinary Analysis and Optimization, 2002-5486.

[20] H. Ou, B. Lu, Z. S. Cui, C. Lin, A direct shape optimization approach for contact problems with boundary stress concentration, Journal of Mechanical Science and Technology 27 (9) (2013) 2751–2759.

[21] D. Brujic, M. Ristic, M. Mattone, P. Maggiore, G. P. De Poli, CAD based shape optimization for gas turbine component design, Structural and multidisciplinary optimization 41 (4) (2010) 647–659.

[22] G. Zboinski, Physical and geometrical non-linearities in contact problems of elastic turbine blade attachments, Proceedings of the Institution of Mechanical Engineers, Part C: J. of Mechanical Engineering Science 209 (4) (1995) 273–286.

[23] A. S. Deshpande, J. A. Keane, A. Sobester, J. J. D. Toal, Geometric parameterisation of firtree joints in gas turbine discs considering manufacturing variability, in: Proceedings of 3rd Aircraft Structural Design Conference, 2012, pp. 470–478.

[24] F. Qin, L. Chen, Y. Li, X. Zhang, Fundamental frequencies of turbine blades with geometry mismatch in fir-tree attachments, J. of Turbomachinery 128 (3) (2006) 512–516.

[25] J. Avalos, M. P. Mignolet, C. Soize, Response of bladed disks with mistuned blade-disk interfaces, in: *Proc. of the ASME Turbo Expo*. GT2009-59580. Orlando, Florida, USA, June 8–12, 2009.

[26] M. Bounazef, S. Guessasma, E. A. Adda Bedia, Blade protection and efficiency preservation of a turbine by a sacrificial material coating, Advanced Powder Technology 18 (2) (2007) 123–133.

[27] P. Song, M. P. Mignolet, Maximum entropy-based uncertainty modeling at the finite element level, in: 2018 AIAA Non-Deterministic Approaches Conference, AIAA SciTech Forum, AIAA2018-1657, 2018.

[28] L. Breiman, Random forests, Machine Learning 45 (1) (2001) 5–32.

[29] J. Ling, A. Ruiz, G. Lacaze, J. Oefelein, Uncertainty analysis and data-driven model advances for a jet-in-crossflow, J. of Turbomachinery 139 (2) (2017) 021008(1–9).

[30] J. Ling, J. Templeton, Evaluation of machine learning algorithms for prediction of regions of high reynolds averaged navier stokes uncertainty, Physics of Fluids 27 (8) (2015) 085103.

[31] C. J. C. Burges, A tutorial on support vector machines for pattern recognition, Data Mining and Knowledge Discovery 2 (2) (1998) 121–167.

[32] S. Trehan, K. T. Carlberg, L. J. Durlofsky, Error modeling for surrogates of dynamical systems using machine learning, Int. J. for Numerical Methods in Engineering 112 (12) (2017) 1801–1827.

[33] I. Mezić, T. Runolfsson, Uncertainty propagation in dynamical systems, Automatica 44 (12) (2008) 3003–3013.

[34] T. West, C. Gumbert, Multifidelity, multidisciplinary design under uncertainty with non-intrusive polynomial chaos, in: 58th AIAA/ASCE/AHS/ASC Structures, Structural Dynamics, and Materials Conference, AIAA 2017-1936, 2017.

[35] A. M. Panunzio, L. Salles, C. Schwingshackl, M. Gola, Asymptotic numerical method and polynomial chaos expansion for the study of stochastic non-linear normal modes, in: *Proc. of the ASME Turbo Expo*. GT2015-43560. Montreal, Cananda, June 15-19, 2015.

[36] A. Sinha, Computation of the statistics of forced response of a mistuned bladed disk assembly via polynomial chaos, Journal of Vibration and Acoustics, Transactions of the ASME 128 (4) (2006) 449–457.

[37] R. Rahul, E. P. Petrov, Analysis of deformation of mistuned bladed disks with friction and random crystal anisotropy orientation using gradient-based polynomial chaos expansion, in: *Proc. of the ASME Turbo Expo*. GT2018-76566. Oslo, Norway, June 11-15, 2018.

[38] A. Saltelli, M. Scott, Guest editorial: The role of sensitivity analysis in the corroboration of models and itslink to model structural and parametric uncertainty, Reliability Engineering & System Safety 57 (1) (1997) 1 – 4.

[39] E. Petrov, Analysis of sensitivity and robustness of forced response for nonlinear dynamic structures, Mechanical Systems and Signal Processing 23 (1) (2009) 68–86.

[40] E. Petrov, A sensitivity-based method for direct stochastic analysis of nonlinear forced response for bladed disks with friction interfaces, Journal of Engineering for Gas Turbines and Power 130 (2008) 022503(1)–022503(9).

[41] Z. Kala, J. Valeš, Global sensitivity analysis of lateral-torsional buckling resistance based on finite element simulations, Engineering Structures 134 (2017) 37–47.

[42] S. H. Hesse, D. H. J. A. Lukaszewicz, F. Duddeck, A method to reduce design complexity of automotive composite structures with respect to crashworthiness, Composite Structures 129 (2015) 236–249.

[43] A. Saltelli, P. Annoni, How to avoid a perfunctory sensitivity analysis, Environmental Modelling & Software 25 (12) (2010) 1508–1517.

[44] R. I. Cukier, H. B. Levine, K. E. Shuler, Nonlinear sensitivity analysis of multiparameter model systems, J. of Computational Physics 26 (1) (1978) 1–42.

[45] I. M. Sobol, Global sensitivity indices for nonlinear mathematical models and their monte carlo estimates, Mathematics and Computers in Simulation 55 (1–3) (2001) 271–280.

[46] B. Sudret, Global sensitivity analysis using polynomial chaos expansions, Reliability Engineering & System Safety 93 (7) (2008) 964–979.

[47] G. Antinori, F. Duddeck, A. Fischersworring-Bunk, Sensitivity analysis and uncertainty quantification for a coupled secondary air system thermomechanical model of a jet engine low pressure turbine rotor, in: Proc. of the 2nd Int. Conf. on Vulnerability and Risk Analysis and Management, (ICVRAM, 2014) and the 6th Int. Sym. on Uncertainty Modeling and Analysis (ISUMA, 2014), pp. 1543–1553.

[48] L. Torgo, Inductive learning of tree-based regression models, Ai Communications 13 (2) (2000) 137–138.

[49] T. Hastie, J. Friedman, R. Tibshirani, Additive Models, Trees, and Related Methods, Springer New York, New York, NY, 2001, pp. 257–298.

[50] F. Pedregosa, G. Varoquaux, A. Gramfort, V. Michel, B. Thirion, O. Grisel, M. Blondel, P. Prettenhofer, R. Weiss, V. Dubourg, J. Vanderplas, A. Passos, D. Cournapeau, M. Brucher, M. Perrot, E. Duchesnay, Scikit-learn: Machine learning in Python, Journal of Machine Learning Research 12 (2011) 2825–2830.

[51] E. Petrov, R. Vitali, R. Haftka, Optimization of mistuned bladed discs using gradient-based response surface approximations, 41st Structures, Structural Dynamics, and Materials Conference, AIAA-2000-1522.

[52] O. Roderick, M. Anitescu, P. Fischer, Polynomial regression approaches using derivative information for uncertainty quantification, Nuclear Science and Engineering 164 (2) (2010) 122–139.

[53] G. Dhondt, CalculiX CrunchiX user's manual version 2.12, in: URL http:www.dhondt.de/ccx_2.12.pdf, 2017.

[54] A. Koscso, G. Dhondt, E. P. Petrov, High-fidelity sensitivity analysis of modal properties of mistuned bladed disks regarding material anisotropy, in: *Proc. of the ASME Turbo Expo*. GT2018-76572. Oslo, Norway, June 11-15, 2018.

[55] A. Saltelli, P. Annoni, I. Azzini, F. Campolongo, M. Ratto, S. Tarantola, Variance based sensitivity analysis of model output. design and estimator for the total sensitivity index, Computer Physics Communications 181 (2) (2010) 259 – 270.

[56] J. Feinberg, H. P. Langtangen, Chaospy: An open source tool for designing methods of uncertainty quantification, Journal of Computational Science 11 (Supplement C) (2015) 46 – 57.